

ORIGIN OF MULTIPLE NUCLEI IN ULTRALUMINOUS INFRARED GALAXIES

HIDENORI MATSUI¹, TAKAYUKI R. SAITOH^{2,3}, JUNICHIRO MAKINO^{1,2,3}, KEIICHI WADA⁴, KOHJI TOMISAKA^{1,2},
 EIICHIRO KOKUBO^{1,2}, HIROSHI DAISAKA⁵, TAKASHI OKAMOTO⁶, AND NAOKI YOSHIDA⁷

¹ Center for Computational Astrophysics, National Astronomical Observatory of Japan, 2-21-1 Osawa, Mitaka, Tokyo 181-8588, Japan

² Division of Theoretical Astronomy, National Astronomical Observatory of Japan, 2-21-1 Osawa, Mitaka, Tokyo 181-8588, Japan

³ Interactive Research Center of Science, Tokyo Institute of Technology, 2-21-1 Ookayama, Meguro, Tokyo 152-8551, Japan

⁴ Graduate School of Science and Engineering, Kagoshima University, 1-21-35 Korimoto, Kagoshima 890-0065, Japan

⁵ Graduate School of Commerce and Management, Hitotsubashi University, Naka 2-1 Kunitachi, Tokyo 186-8601, Japan

⁶ Center for Computational Sciences, University of Tsukuba, 1-1-1 Tennodai, Tsukuba, Ibaraki 305-8577, Japan

⁷ Institute for the Physics and Mathematics of the Universe, University of Tokyo, 5-1-5 Kashiwanoha, Kashiwa, Chiba 277-8583, Japan

Received 2011 January 25; accepted 2011 November 8; published 2012 January 20

ABSTRACT

Ultraluminous infrared galaxies (ULIRGs) with multiple (≥ 3) nuclei are frequently observed. It has been suggested that these nuclei are produced by multiple major mergers of galaxies. The expected rate of such mergers is, however, too low to reproduce the observed number of ULIRGs with multiple nuclei. We have performed high-resolution simulations of the merging of two gas-rich disk galaxies. We found that extremely massive and compact star clusters form from the strongly disturbed gas disks after the first or second encounter between the galaxies. The mass of such clusters reaches $\sim 10^8 M_\odot$ and their half-mass radii are 20–30 pc. Since these clusters consist of young stars, they appear as several bright cores in the galactic central region ($\sim \text{kpc}$). The peak luminosity of these clusters reaches $\sim 10\%$ of the total luminosity of the merging galaxy. These massive and compact clusters are consistent with the characteristics of the observed multiple nuclei in ULIRGs. Multiple mergers are not necessary to explain multiple nuclei in ULIRGs.

Key words: galaxies: evolution – galaxies: interactions – galaxies: starburst – methods: numerical

1. INTRODUCTION

Ultraluminous and luminous infrared galaxies (ULIRGs/LIRGs) have strong infrared (IR) luminosities of $L_{\text{IR}} > 10^{12} L_\odot$ and $10^{11} L_\odot \leq L_{\text{IR}} \leq 10^{12} L_\odot$, respectively (Sanders & Mirabel 1996). Their intense IR luminosities are mainly due to starburst activities, and the contribution of active galactic nuclei (AGNs) to IR luminosity seems to be rather limited, i.e., $\sim 20\%$ (Risaliti et al. 2006; Farrah et al. 2007; Nardini et al. 2008). The starburst activities in (U)LIRGs are likely to be triggered by merging of galaxies, in particular gas-rich galaxies, since observations suggest that (U)LIRGs have complex and disturbed morphologies (Sanders & Mirabel 1996). In the *I*-band (F814W filter) images of 100 sampled (U)LIRGs at $0.05 < z < 0.20$ taken with *Hubble Space Telescope* (HST), about 20% of ULIRGs have multiple (≥ 3) nuclei (Borne et al. 2000; Cui et al. 2001). The fraction increases to more than 80% if all probable galaxies are included (Borne et al. 2000).

The origin of the multiple nuclei has been thought to be multiple major merger events. In order to explain multiple mergers, Borne et al. (2000) argued that the progenitors of (U)LIRGs were compact groups of galaxies. However, the evolution timescale of compact groups is very long ($\sim H_0^{-1}$; Athanassoula et al. 1997). Therefore, the probability that two galaxies merge in a compact group and the merging galaxy has double cores is $p_{\text{pair}} \sim t_{\text{merg}}/H_0^{-1} \sim 100 \text{ Myr}/10 \text{ Gyr} \sim 0.01$, where t_{merg} is the merging timescale of the galactic cores. The probability that another galaxy merges with such a merging galaxy in the compact group and the merging galaxy has triple cores is $p_{\text{multi}} = p_{\text{pair}} \times (1/N_g - 2) \times p_{\text{pair}} \sim 3 \times 10^{-5}$, where N_g (~ 5) is the typical number of galaxies in a compact group (Mendes de Oliveira & Hickson 1991). Then, the number density of ULIRGs with multiple cores is $\phi_g \times p_{\text{multi}} \sim 3 \times 10^{-9} \text{ Mpc}^{-3}$, where ϕ_g ($\sim 10^{-4} \text{ Mpc}^{-3}$) is the number density of galaxies

in a compact group (Mendes de Oliveira & Hickson 1991; Ribeiro et al. 1994). Since the number density of ULIRGs is 10^{-7} Mpc^{-3} (Sanders et al. 2003), the fraction of multiple mergers to ULIRGs is $(3 \times 10^{-9})/10^{-7} \sim 0.03$. Thus, it is unlikely that multiple merger is a major cause of the observed multiple nuclei in (U)LIRGs. An alternative explanation for the origin of multiple nuclei in (U)LIRGs seems necessary.

Previous numerical simulations of merging galaxies (Mihos et al. 1992; Mihos & Hernquist 1996; Barnes & Hernquist 1996; Kazantzidis et al. 2005; Cox et al. 2006; Di Matteo et al. 2007; Narayanan et al. 2009; Covington et al. 2010) have shown that starbursts occurred during the merging process. However, these simulations failed to reproduce the formation of star clusters as observed in many interacting and merging galaxies (Whitmore & Schweizer 1995; Mengel et al. 2008) since their spatial and mass resolutions (e.g., 100 pc and $\sim 10^6 M_\odot$) were not sufficiently high to distinguish star-forming regions and formation of star clusters whose sizes are less than 100 pc. In addition, previous simulations did not allow the interstellar medium (ISM) to cool below $\sim 10^4 \text{ K}$. This is another reason why formation of star clusters was not reproduced in the previous simulations.

In order to reproduce formation of star clusters, high-resolution simulations have been attempted. Li et al. (2004) have performed the simulation of a merging galaxy using the Tree+SPH code GADGET. In this simulation, mass and spatial resolutions were 10 pc and $6.6 \times 10^3 M_\odot$, respectively. They assumed an isothermal ISM and used sink particles, which absorb their surrounding gas, to represent clusters. They have shown that a number of massive clusters form in the merging process. In this simulation, the most massive cluster has a mass of $7.8 \times 10^7 M_\odot$. Bournaud et al. (2008) have performed simulations of merging galaxies using sticky particles, which collide inelastically, instead of solving hydrodynamics. In these simulations, mass and spatial resolutions were 32 pc and $7 \times 10^3 M_\odot$,

respectively. They have also shown formation of massive star clusters with masses of $10^{5-7} M_{\odot}$. These simulations are, however, unrealistic in the sense that dynamical evolution of star clusters themselves cannot be properly followed due to the limitation of the sticky and sink particle methods. Saitoh et al. (2009) improved the spatial and mass resolutions ($5\text{--}20\text{ pc}$ and $10^{3-4} M_{\odot}$) and allowed the ISM model to cool to 10 K . These simulations showed that the behavior of the multiphase ISM in the merging galaxy is considerably altered and the formation of shock-induced star clusters is naturally reproduced (Saitoh et al. 2009, 2011). There are several high-resolution simulations of merging galaxies which resolve the low-temperature gas ($300\text{--}500\text{ K}$) using adaptive mesh refinement methods (Kim et al. 2009; Teyssier et al. 2010). These simulations also showed the difference in the behavior of the multiphase ISM compared with the ISM used in the previous simulations. Kim et al. (2009) considered the merger of low-mass galaxies ($\sim 1.8 \times 10^{10} M_{\odot}$). Several spiky peaks of star formation rate (SFR) were seen in their simulation although the most prominent starburst was found at the beginning of the simulations and a significant fraction of the ISM was blown away by energetic wind before the merging event. Thus, it would be hard to investigate the detailed evolution of the ISM in merging galaxies. In Teyssier et al. (2010), the polytropic equation of state was used instead of solving the energy equation, which is essentially different from Saitoh et al. (2009) and the present paper. The validity of this approximation is unclear for understanding the evolution of the ISM in merging galaxies.

High-resolution images of the local (U)LIRGs obtained by integral field spectroscopy using the William Herschel Telescope (García-Marín et al. 2009a, 2009b) and VLT-VIMOS (Alonso-Herrero et al. 2009, 2010; Monreal-Ibero et al. 2010; Rodríguez Zaurín et al. 2010) showed that (U)LIRGs generally have very complex structures, such as $H\alpha$ bright knots, rings, and tidal tails. As in the case of formation of star clusters, the reason why these structures have not been reproduced in numerical simulations might simply be the inadequate treatment of the ISM and limited resolution. Thus, high-resolution simulations resolving a multiphase ISM are essential to comprehend the complex structures in (U)LIRGs.

We have performed high-resolution simulations of merging galaxies with sufficiently high spatial resolution and a cooling function for the ISM that covers a wide range of temperature ($10\text{ K} < T < 10^8\text{ K}$). In this paper, we focus on the origin of the observed ULIRGs with multiple nuclei. The detailed evolution of merging galaxies will be described in forthcoming papers.

The structure of this paper is as follows. We first describe the numerical methods and models in Section 2. Numerical results are shown in Section 3. In Section 4, we compare our results with observations. Conclusions and discussion are presented in Section 5.

2. METHODS

2.1. Simulation Setup

The model parameters of the initial disk galaxy are the same as those used in Saitoh et al. (2009). The masses of the dark matter halo and old stellar and gas disks are $1.1 \times 10^{11} M_{\odot}$, $5.1 \times 10^9 M_{\odot}$, and $1.2 \times 10^9 M_{\odot}$, respectively. The gas fraction in the disk is $\sim 20\%$ of the total disk mass. The gas fraction is set to be slightly higher than that of local spiral galaxies since the gas fraction decreases due to star formations during the isolated phase for 1 Gyr before the interactions (see below).

We also assume the halo gas component has a total mass of $1.1 \times 10^9 M_{\odot}$. It has the same distribution as the dark matter halo. The initial gas temperatures are 10^4 K in the disk and 10^5 K in the halo. The scale radii of the stellar and gas disks are 4 kpc and 8 kpc , respectively. The dark matter halo and the stellar disk are expressed by N -body particles, whereas the gas disk is expressed by smoothed particle hydrodynamics (SPH) particles.

Unlike Saitoh et al. (2009), before starting the simulations, we let an isolated disk galaxy evolve for 1 Gyr in order to stabilize the gas component. After this evolution, the amount of disk and halo gas in each galaxy is $1.8 \times 10^9 M_{\odot}$. The SFR during this period is $\sim 0.5 M_{\odot} \text{ yr}^{-1}$. During the first 1 Gyr, the disk galaxy holds a quasi-steady state and is free from a global instability due to gravity. The evolution of the isolated disk is different from that of a gas-rich disk at high z . Simulations of the gas-rich disk, in which the gas mass fraction of the disk is $\geq 50\%$, have shown that massive clumps form from the gravitational instability of the gas-rich disk (Noguchi 1999; Immeli et al. 2004; Bournaud et al. 2007). In contrast to the simulations of merging of such clumpy disks at high z by Bournaud et al. (2011), we focus on the merging process of two local disk galaxies.

We let the two pre-evolved galaxies collide in a parabolic orbit with a pericentric distance of 7.5 kpc . The simulations start with an initial separation of 75 kpc , where the separation distance is measured between the mass centers of the two galaxies.

We have performed nine runs. Three are high-resolution runs (H_{XX} in Table 1) and the rest are low-resolution runs (L_{XX}). The initial masses of SPH, star, and dark matter particles are the same. They are $7.5 \times 10^3 M_{\odot}$ and $3 \times 10^4 M_{\odot}$ for H_{XX} and L_{XX} runs, respectively. Subscripts P, T, and R denote prograde, tilted, and retrograde spin axes of the two galaxies. We performed six possible combinations of the spin orientations in low resolution and only PP and TT cases in high resolution. The gravitational softening length, ϵ , is set to be 20 pc for eight runs while for the $H_{TT,5\text{ pc}}$ run the softening length is 5 pc .

The orientation of the disk axis is specified by two angles, i and ω . Here, i is the inclination and ω is the argument of the pericenter. They are defined as follows. We use the coordinate system in which the orbital plane of the two galaxies is in the x - y plane. The Laplace–Runge–Lenz vector of the orbit is $\mathbf{e}_p = (1, 0, 0)$. The spin axis of a galaxy is then given by $\mathbf{e}_g = (\sin \omega \sin i, \cos \omega \sin i, \cos i)$. These angles are defined relative to the orbit of each galaxy. Thus, in the case of “TT” runs, the spin axes of the two galaxies are parallel to each other.

2.2. Numerical Method

Numerical simulations were performed by an N -body/SPH code ASURA (Saitoh et al. 2009) that can optionally utilize GRAPE (Sugimoto et al. 1990) in order to accelerate calculation of the gravitational force. We adopted a time-step limiter (Saitoh & Makino 2009) for the time integration of SPH particles with individual time steps, which keeps the differences in time steps of neighboring particles small enough to handle the strong shocks correctly. We also used the FAST scheme (Saitoh & Makino 2010) that allows self-gravitating SPH particles to use different time steps for integrations of hydrodynamics and gravity. This method accelerates simulations without losing the accuracy of the time integration. The leapfrog method is used for the time integrations of both gravity and hydrodynamics. These improvements allow us to follow the formation of cold and dense gas clumps and their expansion by supernovae (SNe) feedback without numerical problems.

Table 1
The Model Parameters

Run	i_1^a (deg)	ω_1^b (deg)	i_2^c (deg)	ω_2^d (deg)	m^e (M_\odot)	N_{SPH}^f	N_{star}^g	N_{DM}^h	ϵ^i (pc)
H_{PP}	0	...	0	...	7.5×10^3	514476	1841042	27720000	20
H_{TT}	-109	-30	71	-30	7.5×10^3	514476	1841042	27720000	20
L_{PP}	0	...	0	...	3.0×10^4	133696	447994	6930000	20
L_{PR}	0	...	180	...	3.0×10^4	133696	447994	6930000	20
L_{RR}	180	...	180	...	3.0×10^4	133696	447994	6930000	20
L_{PT}	0	...	71	30	3.0×10^4	133696	447994	6930000	20
L_{TR}	-109	30	180	...	3.0×10^4	133696	447994	6930000	20
L_{TT}	-109	-30	71	-30	3.0×10^4	133696	447994	6930000	20
$H_{\text{TT},5\text{ pc}}$	-109	-30	71	-30	7.5×10^3	514476	1841042	27720000	5

Notes.

^a The disk inclination for the galaxy 1.

^b The argument of the pericenter for the galaxy 1.

^c The disk inclination for the galaxy 2.

^d The argument of the pericenter for the galaxy 2.

^e The mass of SPH, star, and dark matter particles.

^f The number of SPH particles.

^g The number of star particles.

^h The number of dark matter particles.

ⁱ The gravitational softening length.

For the radiative cooling and heating, we follow the treatment of Saitoh et al. (2008) in which the gas is allowed to cool down to 10 K. The treatments of star formation and SN feedback are also the same as those in Saitoh et al. (2009). When an SPH particle satisfied (1) a high number density ($n_{\text{H}} > 100 \text{ cm}^{-3}$), (2) a low temperature ($T < 100 \text{ K}$), and (3) a collapsing region ($\nabla \cdot \mathbf{v} < 0$), the SPH particle spawns a star particle whose mass is one-third of the original SPH particle mass. We assume a simple stellar population approximation for newly formed star particles. Salpeter’s initial mass function with mass range $0.1\text{--}100 M_\odot$ is adopted (Salpeter 1955). Stars with mass $\geq 8 M_\odot$ in each star particle explode as Type II SNe and release 10^{51} erg of thermal energy per SN into the surrounding ISM.

3. MULTIPLE NUCLEI IN ULIRGs

Initially, the two galaxies move on parabolic orbits and approach each other. At around $t = 450 \text{ Myr}$, they reach the pericenter (first encounter). Since the orbital angular momenta of their main bodies are converted into the disk internal spin, they lose their orbital angular momenta (Barnes 1992; Hernquist 1992, 1993; Mihos & Hernquist 1996) and their trajectories deviate from the parabolic orbits. The main bodies approach each other again (second encounter). Finally, after several encounters, their cores completely merge.

Figures 1 and 2 show the evolution of the distribution of gas and stellar particles for runs H_{PP} and H_{TT} . Gas disks are strongly disturbed at the first encounter (the panels at $t = 430$, 463, and 596 Myr) and at the second encounter (the panels at $t = 830$ and 863 Myr) in run H_{PP} and at the second encounter (the panels at $t = 863$ and 896 Myr) in run H_{TT} . Because of the strong perturbation, gas is compressed by large-scale shocks. The dense gas radiatively cools and becomes gravitationally unstable. As a result, massive star clusters form (see also Saitoh et al. 2010, 2011).

Figure 3 shows the synthesized I -band images from our merger simulations after the massive star clusters formed. Here, the I -band luminosity emitted from newly formed stars was calculated using the population synthesis code PÉGASE (Fioc & Rocca-Volmerange 1999), and effects of dust absorption and

re-emission were neglected. The two top panels show the high-resolution runs and the six lower panels show the low-resolution runs. In all images, multiple compact sources appear in the central regions of galaxies. The two indicated by arrows are the progenitor galactic cores and the others are newly formed massive star clusters. The absolute magnitudes of these clusters in I band are $M_I \lesssim -17.0$, comparable to those of the galactic central cores. The effect of dust extinction is discussed in Section 4.2.

Since the cores form through the gravitational instability of strongly perturbed gas disks, they do not contain dark matter and consist only of young stars. On the other hand, the galactic luminous nuclei contain dark matter and a large amount of old stars that have formed before the merger event. The properties of newly formed cores are, therefore, different from those of the galactic nuclei. In addition, such cores are more massive by an order of magnitude than usual star clusters with $10^{6-7} M_\odot$. We therefore call the newly formed cores “hypermassive star clusters.” Since the hypermassive star clusters form in the galactic central region ($\sim \text{kpc}$), they are different from tidal dwarfs that are formed in tidal arms (e.g., Barnes & Hernquist 1992; Bournaud et al. 2008).

The reason why they are extremely massive can be explained as follows. The total mass of the gas which becomes gravitationally unstable is very large ($\sim 1.0 \times 10^9 M_\odot$) because of the strong large-scale gravitational and hydrodynamical disturbances from another galaxy at the encounter phase. The strong disturbances deform the gravitational potential into a strongly non-axisymmetric shape. Therefore, the rotation of the disk becomes ineffective in stabilizing long-wavelength perturbations. Even though the gas disk fragments into a number of small clumps with $\sim 10^{6-7} M_\odot$, these small clumps are still gravitationally bound to each other and eventually merge to form larger clusters.

Figure 4 shows snapshots during the formation of the most massive cluster from 900 Myr to 913 Myr in run H_{TT} . Multiple gas clumps formed from the disturbed gas disk merge with each other and become one massive cluster. In other words, the merging of smaller clumps within the short timescale

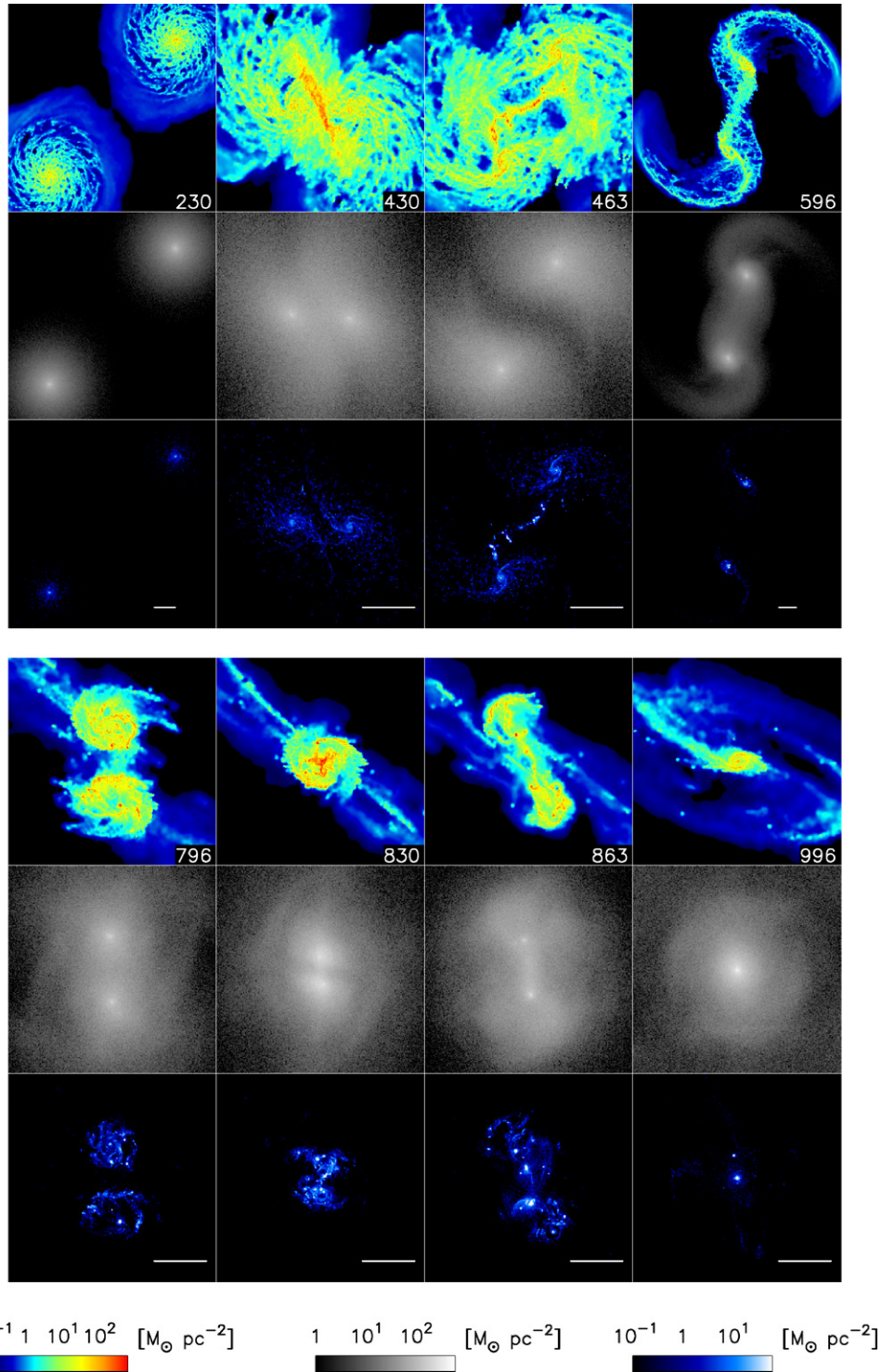


Figure 1. Snapshots of run *Hpp*. The upper color, middle gray scale, and bottom color panels show the surface density of gas, old stars, and newly formed stars that are born after $t = 0$, respectively. In each upper panel, the number in the right-bottom corner displays the simulation time (the unit is Myr). The white line in the right-bottom corner of each panel shows a length of 5 kpc.

causes quick growth of the mass of star clusters. As a result, hypermassive star clusters form.

In Figure 5, we show the evolution of the masses of these hypermassive star clusters (upper panels) and their distances from the closer galactic center (lower panels). The clusters first grow quickly, reaching about half of the final mass in around 20 Myr. After that, the growth in mass slows down and the clusters fall to the center of the galaxy due to dynamical friction.

As a result, the merger remnant has a very compact and luminous core similar to those observed in a large number of elliptical galaxies (e.g., Kormendy et al. 2009).

Figure 6 shows the evolution of the SFR and bolometric luminosity coming from the stars in the merging event. The effects of dust absorption and re-emission are not taken into account. If we take them into account, the IR luminosity would become higher since ultraviolet and optical photons are absorbed

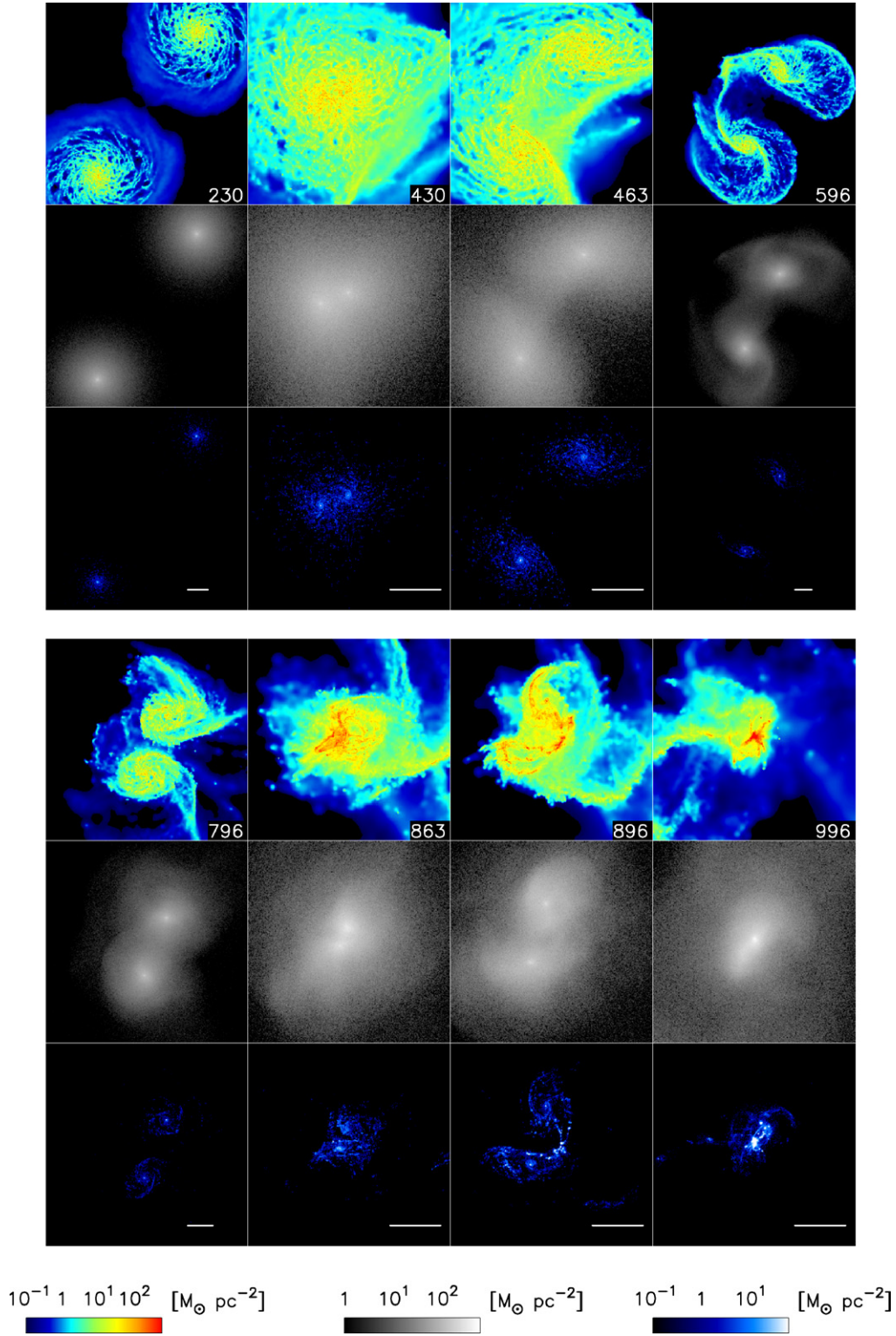


Figure 2. Same as Figure 1 but for run H_{TT} . The snapshots are projected to the disk plane.

by dust and re-emitted in the IR regime. Therefore, we expect that the bolometric luminosity of our runs is a good indicator of the IR luminosity. In all runs, the maximum SFR reaches $20 M_{\odot} \text{ yr}^{-1}$, and the luminosity reaches $10^{11} L_{\odot}$, which is about an order of magnitude higher than that before the encounter. The figure shows that the evolution of bolometric luminosity reflects the SFR. The peak luminosity is comparable to those

of LIRGs (Sanders & Mirabel 1996). If the progenitor galaxies are more massive and/or the initial gas fraction is much higher than those used in this simulation, the peak of the SFR would become higher and the merger galaxy would become an ULIRG with infrared emission $\geq 10^{12} L_{\odot}$. AGNs would also provide an additional IR luminosity, although our simulations do not take into account the effect of AGNs. The influence of AGNs on

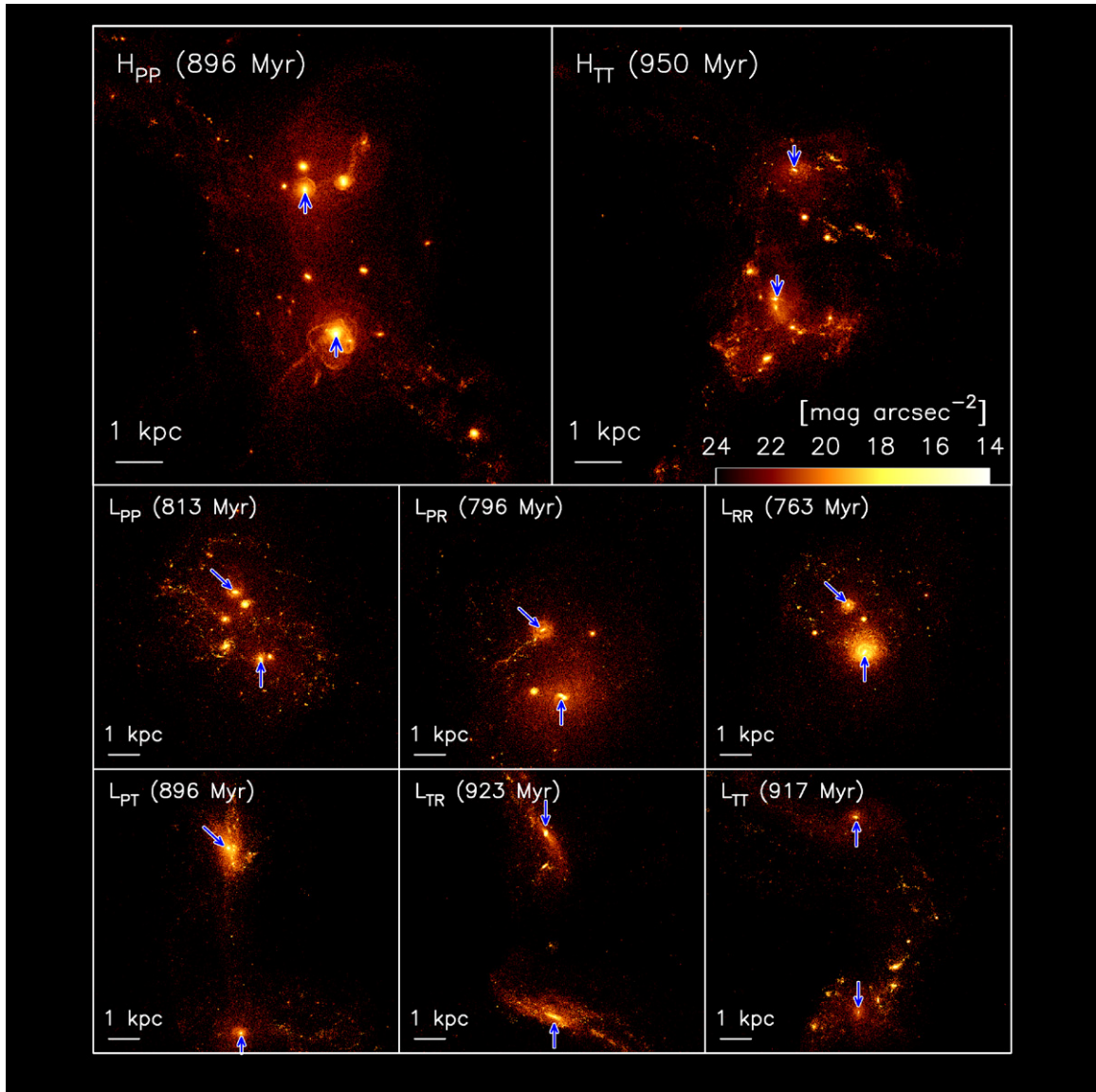


Figure 3. Simulated *HST* WFPC2 *I*-band (F814W filter) images from our simulations. The color represents magnitude per square arcsec. The left and right panels in the top row show the results of runs H_{PP} and H_{TT} , respectively. These two runs are simulated with high resolution. The six panels in the bottom two rows show the results of low-resolution runs. We ignore the effect of dust extinction (see Section 4.2.).

the total IR luminosity is typically $\sim 20\%$ of the total (Risaliti et al. 2006; Farrah et al. 2007; Nardini et al. 2008). The peak mass-to-light ratio of our run, M/L , is less than 0.1 and is comparable to that of ULIRGs (Colina et al. 2005; Hinz & Rieke 2006). The period of the high-luminosity phase is ~ 200 Myr. The hypermassive star clusters after their formation contain a large amount of dusty gas and young stars as shown in Figure 4. Therefore, strong infrared emission from the hypermassive star clusters is likely to be observable.

In order to study the dependence on the numerical resolution of the formation of hypermassive star clusters, we have performed simulations with different mass resolutions. In both high- and low-resolution runs, hypermassive star clusters with $\sim 10^8 M_\odot$ are formed as shown in Figure 3. Their formation process is the same as that of the high-resolution runs. In addition, the time evolution of the SFR is also similar to that of the high-resolution runs. In both runs, the peak of the SFR is $20\text{--}30 M_\odot \text{ yr}^{-1}$ and the duration time of active star formation is about 200 Myr.

4. COMPARISON WITH OBSERVATIONS

4.1. Surface Brightness and Spatial Distribution of Multiple Nuclei

Here, we compare our numerical results with observations of ULIRGs with nuclei. Cui et al. (2001) observed nuclei with absolute magnitude from -17 to -21 in the *I* band. The *I*-band luminosity of the identified putative nuclei is typically around a few percent of the far-infrared luminosity of their host galaxy (Cui et al. 2001).

We estimated the absolute *I*-band magnitude of hypermassive star clusters formed in our simulations using PÉGASE. Some hypermassive star clusters have luminosity comparable to the observed putative nuclei. In the upper panels of Figure 3, there is one hypermassive star cluster with $M_I \sim -17.4$ in run H_{PP} , and there are three hypermassive star clusters with $M_I \sim -17.7$, -17.1 , and -17.1 in run H_{TT} , respectively. These *I*-band absolute magnitudes are comparable to those of the galactic cores, which are -18.5 and -17.5 in run H_{PP} and -17.7

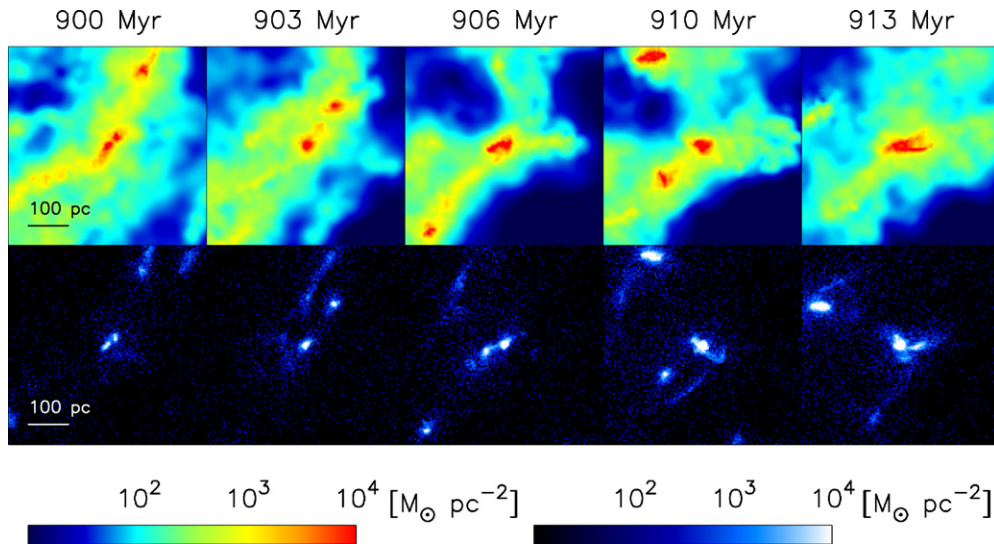


Figure 4. Formation of the most massive star cluster in run H_{TT} (the black curve in the right panels of Figure 5). The upper panels show the evolution of the gas surface density while the lower ones display that of the stellar surface density. The size of each panel is 500 pc by 500 pc and its center is taken as the center of mass of the main progenitor of the final cluster. Two clusters in the center of the panel at 900 Myr have merged at 903 Myr. Two clusters at 903 Myr approach and merge with each other at 906 Myr. The cluster in the left-bottom corner of the panel at 906 Myr merges with the cluster at the center by 913 Myr.

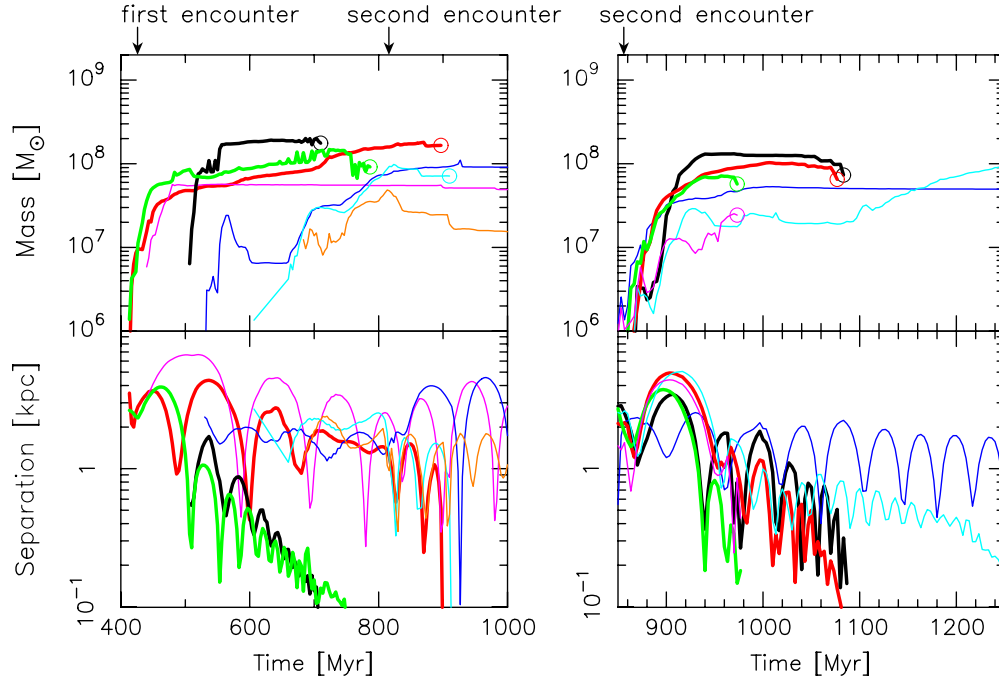


Figure 5. Time evolution of masses of hypermassive star clusters (upper panels) and their distances from the galactic center (lower panels). The galactic center is given by the nearest one to the cluster before the coalescence of galactic cores and by the galactic center of a merger remnant after that. The left and right panels show the result of runs H_{PP} and H_{TT} , respectively. The three most massive star clusters are shown by the thick curves and the others are shown by the thin curves. We show the evolution of each cluster until it sinks to the galactic center (the distance becomes less than 100 pc) or it is disrupted by tidal forces (Saitoh et al. 2006). Once they sink to the galactic center at less than 100 pc or one fully disrupted by the tidal force, we put circles at these points and stop tracing their evolutions.

and -15.7 in run H_{TT} . These results indicate that the galactic nuclei and hypermassive star clusters are not distinguishable by their luminosities. The I -band (bolometric) luminosity of hypermassive star clusters is a few percent ($\gtrsim 10\%$) of the bolometric luminosity of the host galaxy with $\sim 10^{11} L_{\odot}$. These characteristics are in good agreement with the observations.

We also compare the spatial distribution of the observed putative nuclei with that of simulated hypermassive star clusters. If we select relatively compact ULIRGs, the average separation between nuclei is about 1 kpc (Cui et al. 2001). In our simulations, the separation between hypermassive star clusters and

galactic cores depends on the evolution phase. However, the typical separation is a few kpc in the most luminous phase of the galaxies. Thus, the spatial distribution also agrees with the observations.

4.2. Dust Extinction

In this subsection, we investigate the effect of dust extinction in I -band. Here, we use the high spatial resolution run, $H_{TT,5pc}$, in which the softening length is 5 pc for mock observations, since the detailed structure of the ISM is important to estimate the extinction. In this run, similarly to run H_{TT} , hypermassive

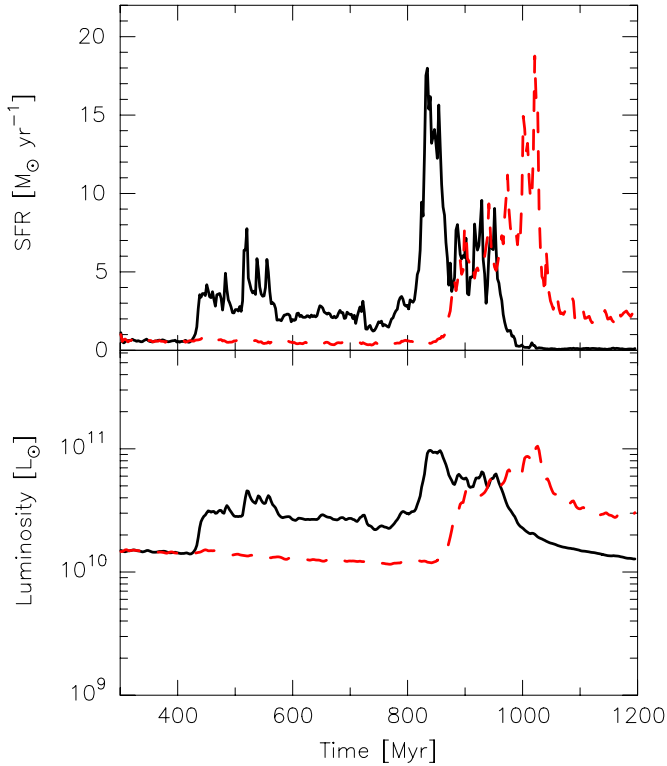


Figure 6. Time evolution of the SFR (upper panel) and the bolometric luminosity (lower panel) of merging galaxies. The black solid and red dashed curves show results of runs H_{PP} and H_{TT} , respectively. We show the mean quantities at each 1 Myr.

star clusters with $\gtrsim 10^8 M_\odot$ form after the second encounter. The masses of the first, second, and third most massive star clusters are $\sim 1.6 \times 10^8 M_\odot$, $1.1 \times 10^8 M_\odot$, and $6.1 \times 10^7 M_\odot$, respectively.

The flux, taking dust extinction into account, from a star is estimated by $F = F_0 \prod_i \exp(-\tau_i)$. Here, F_0 is the flux expected without dust extinction and τ_i is the optical depth for each SPH particle and $\tau_i = q_d \sigma_{H,I} N_{H,i} (Z_i/Z_\odot)$ (Bekki & Shioya 2000; Kobayashi et al. 2010), where q_d , $\sigma_{H,I}$, $N_{H,i}$, and Z_i represent the clumpiness parameter, the dust cross-section per H atom at I band for the Milky Way dust model, column number density of atomic H of an SPH particle, and the metallicity of an SPH particle, respectively. The SPH particles between the star and the observer are used for calculating the optical depth, τ . The clumpiness parameter is introduced in order to represent the clumpiness of the dust distribution in the ISM. It is assumed to be 0.15, 0.5, and 1.0. The value of $q_d = 0.15$ is used in Ly α emitters (Kobayashi et al. 2010), whereas $q_d = 1.0$ is the case without the dust clumpiness under the spatial resolution. Here, we do not estimate the “clumpiness” of SPH particles along the line of sight directly since the “real” clumpiness comes from much smaller scale in the ISM. We adopt $\sigma_{H,I} = 4.0 \times 10^{-22} \text{ cm}^2$ (Draine 2003). The column density of an SPH particle is given by $N_{H,i} = m_i W(r, h)$, where m_i and $W(r, h)$ are the mass and two-dimensional kernel function of the SPH particle, respectively, where r is the two-dimensional distance between the SPH and star particles in the projected plane, and h is the kernel size of the SPH particle.

Figure 7 illustrates the effect of dust extinctions. The upper row shows the time evolution of the I -band map without extinction. The middle row represents the expected observation taking dust extinction with $q_d = 0.5$ into account for run

$H_{TT, 5 \text{ pc}}$. Here, the map is projected onto the orbital plane of the galaxies. After formation of hypermassive star clusters, strong dust extinction takes place in the clusters since there is a large amount of dusty gas. The dust extinction reduces the flux from the formed hypermassive star clusters. The extinction of the clusters in I band is $A(I) \gtrsim 5 \text{ mag}$ in the $q_d = 0.5$ case as shown in the bottom panels of Figure 7. In the models of $q_d = 0.15$ and $q_d = 1.0$, the extinctions are $A(I) \gtrsim 4$ and $A(I) \gtrsim 6$, respectively. The strong extinction continues until 970 Myr (the left and middle panels), which corresponds to the epoch about 50 Myr after the formation of the clusters. In this dusty phase, multiple core structures are buried by dust. After 990 Myr (the right panels), the clusters become optically thin because of consumption of dusty gas by star formation and escape of dusty gas from the cluster by SN feedback. As a result, the multiple cores appear. The extinction becomes $A_I \lesssim 1 \text{ mag}$. On the other hand, the galactic central region is still buried by dust due to the continuous gas accretion. In this phase, the extinction does not depend strongly on the clumpiness parameter since dusty gas is restricted to the central region of the cluster rather than distributed in the broad region of the cluster.

The timescale in which hypermassive star clusters become optically thin in I band is less than the ULIRG lifetime ($\sim 200 \text{ Myr}$ as shown in Figure 6). Therefore, it is possible for the clusters to be observed as ULIRGs. Note, however, that the estimate of the dust extinction depends strongly on the distribution of the dust and that resolutions of current simulations are insufficient to resolve the “real” structure of the ISM. Further high-resolution simulations are necessary to involve the clumpiness of the dust distribution in the ISM.

4.3. The Fraction of ULIRGs with Multiple Nuclei

The fraction of ULIRGs with multiple nuclei strongly depends on the wavelength used for observation. In the analysis of *HST* I -band data of ~ 100 ULIRG samples by Borne et al. (2000) and Cui et al. (2001), the fraction of ULIRGs with multiple nuclei is $\sim 20\%$. In addition, Cui et al. (2001) have analyzed the nine samples of Surace et al. (1998) in I band. Two ULIRGs are found to have multiple nuclei, i.e., the fraction is consistent with the results of Borne et al. (2000) and Cui et al. (2001).

On the other hand, Bushouse et al. (2002) and Veilleux et al. (2002) have claimed that the fraction of ULIRGs with multiple nuclei is less than 5% based on their analysis of the data observed in near-IR bands. Using the *HST* H -band data, Bushouse et al. (2002) reanalyzed 27 samples randomly selected from the 123 I -band samples, which include a part of Borne’s and Cui’s samples with multiple nuclei. In their analysis, only one sample is classified as an ULIRG with multiple nuclei. The other sample includes some ULIRGs that have been already classified as ULIRGs with multiple nuclei by I -band image analysis (Borne et al. 2000; Cui et al. 2001). The reasons for excluding them from ULIRGs with multiple nuclei are as follows: (1) the nucleus seems to locate on the tidal arm and is thought to be the tidal arm or (2) multiple nucleus morphologies do not appear in the H -band images. Furthermore, Veilleux et al. (2002) analyzed the K' -band data of 118 ULIRGs taken by the Keck Observatory. Their samples also include candidates for ULIRGs with multiple nuclei in *HST* I -band data. Some of them are excluded since multiple cores are not apparent in K' band in spite of their appearance in I band. As a result, only five ULIRGs ($\sim 4\%$) are classified as ULIRGs with multiple nuclei.

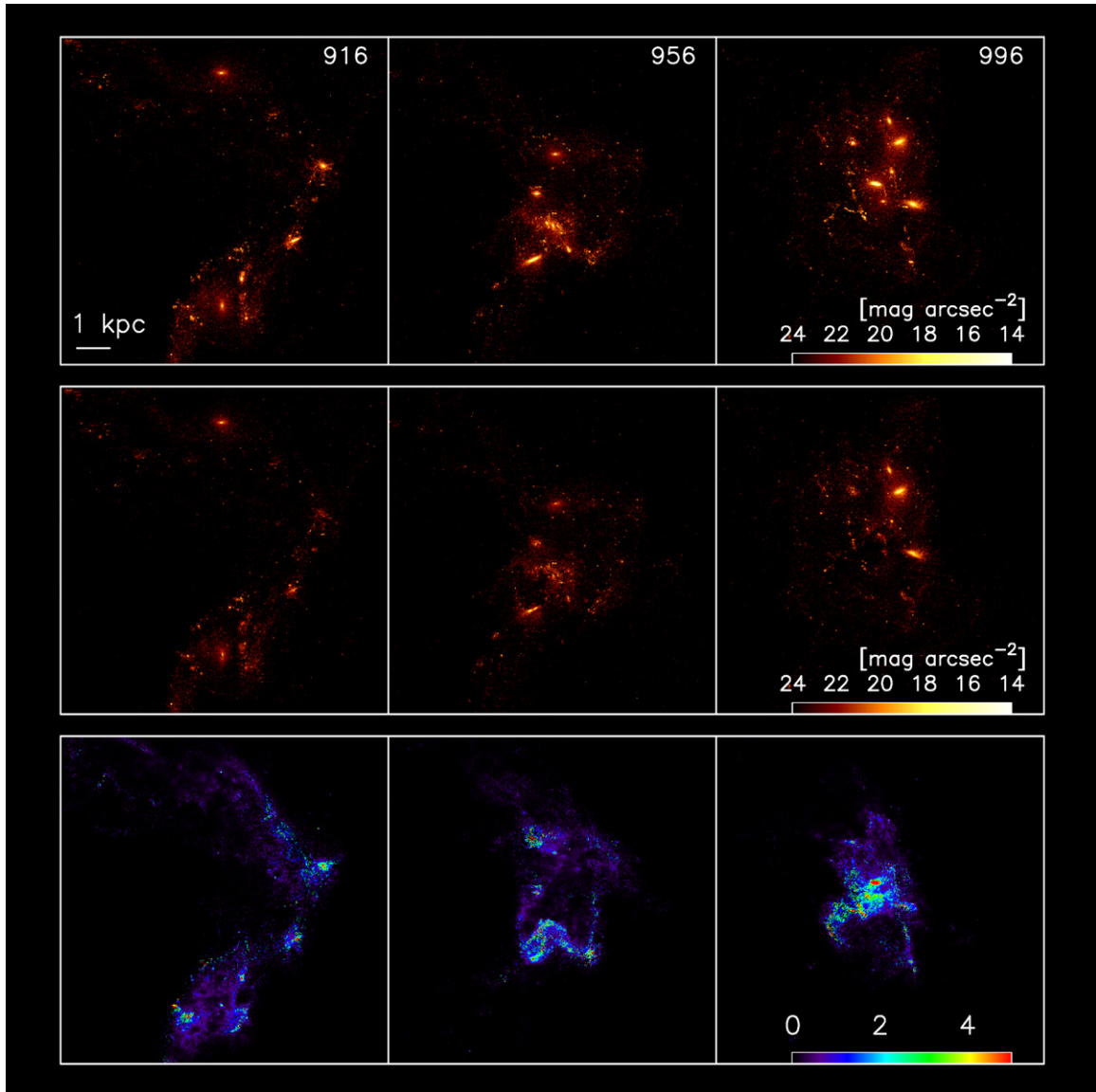


Figure 7. Time evolution of I -band map. The upper panels show the map without dust extinctions and the middle panels show the map taking dust extinction into account. Here, the clumpiness parameter is $q_d = 0.5$. At the upper-right corner in all upper panels, the simulation time (Myr) is shown. The bottom panels show the amount of extinction (the unit is magnitude).

In order to understand the difference between the results obtained using images taken in different bands, we made I -, H -, and K -band images of our simulation data using PÉGASE. We assumed that galaxies were at $z \sim 0.1$ ($1'' \sim 2$ kpc). The point-spread function was assumed to be Gaussian and its dispersion was calculated by $\sigma = \Delta x / \sqrt{2 \ln 2}$, where Δx is the spatial resolution. The spatial resolutions of I - and H -band images were given by the diffraction limit since we assumed the observations by *HST*. The spatial resolutions of I and H bands are $0''.1$ and $0''.2$, respectively. For K -band images, the seeing determines the spatial resolution since we assumed ground-based observations by the University of Hawaii 2.2 m telescope or the Keck spectroscopy. The spatial resolution, therefore, is set to be $0''.5$ (Kim et al. 2002). For comparison, we also made emulated images with K band by *James Web Space Telescope* (*JWST*) or ground-based 8 m telescopes with adaptive optics (AO). We assume that the angular resolution of these future instruments is $\sim 0''.05$.

Figure 8 shows I -, H -, and K -band images, in which dust extinction is not taken into account, of runs H_{PP} and H_{TT} . In I -band images, multiple core-like structures are clearly visible, while such cores are blurred in other bands due to the limited resolution and the contribution of the luminosity of old stars. In H -band images, cores are connected to one another and form arm-like structures. As a result, the cores seem to be in arms. In K -band images, multiple core structures are not resolved at all. As a result, ULIRGs seem to have only single or double cores. Thus, multiple cores were identified as single or double cores in H - and K' -bands. Our analysis indicates that ULIRGs with multiple cores can be misclassified as ones with single or double cores. The apparent discrepancy in the observational fractions of ULIRGs with multiple nuclei might have been caused by this difference in the spatial resolution.

In the rightmost column in Figure 8, we show the emulated K -band images of our simulations with an angular resolution of $0''.05$. We can clearly see the multiple bright sources in these

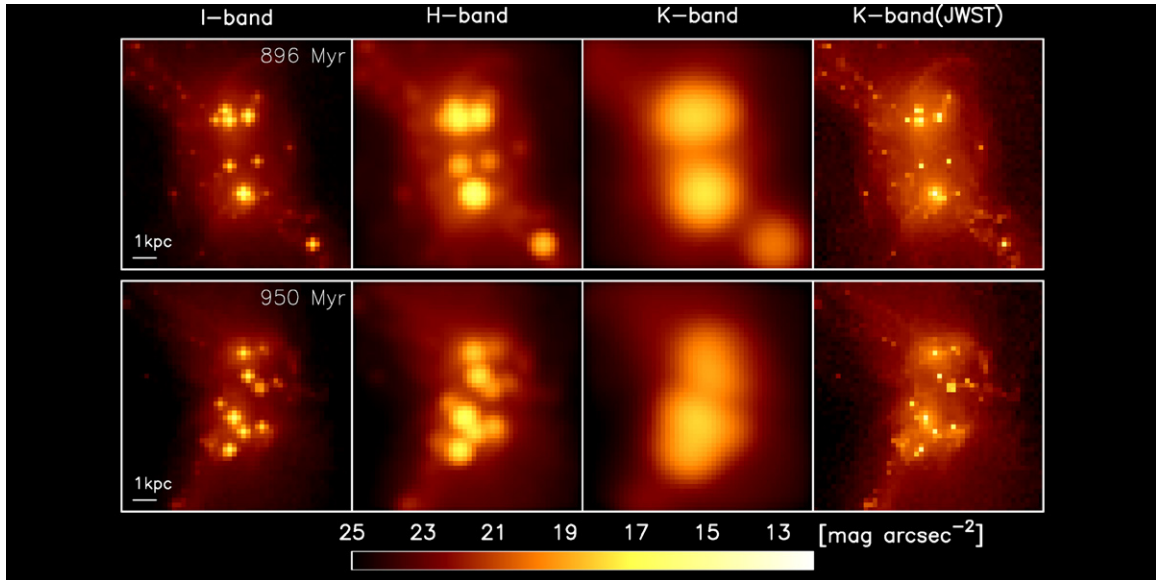


Figure 8. Observed images without dust extinction in our simulations. The upper panels show the images of run H_{pp} and the lower panels show those of run H_{TT} . From left to right, we show images observed by I , H , and K bands with current instruments and K bands with $JWST$. The corresponding angular resolutions for these four bands are $0''.1$, $0''.2$, $0''.5$, and $0''.05$, respectively. See the text for details.

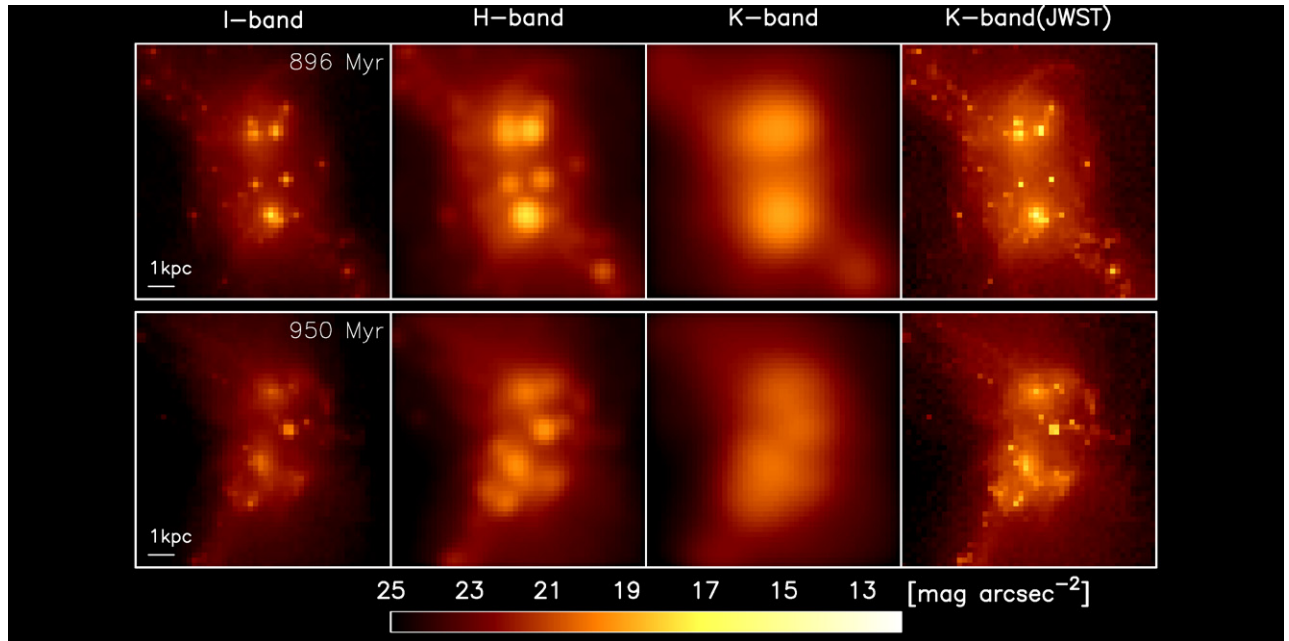


Figure 9. Same as Figure 8 but taking dust extinction into account.

K -band images that were not visible in ground-based observations since the resolution of the image is remarkably improved. We expect that, in the near future, observations of (U)LIRGs by $JWST$ or ground-based 8 m telescopes with AO will settle the problem of the band-to-band difference in the fraction of ULIRGs with multiple nuclei.

Figure 9 shows the observed I -, H -, and K -band images taking dust extinction into account. Here, the cross-sections per H atom at H and K bands are assumed to be $\sigma_{H,H} = 1.0 \times 10^{-22}$ and $\sigma_{H,K} = 7.0 \times 10^{-23}$, respectively (Draine 2003). We adopt $q_d = 0.5$ as a fiducial value. In the I -band image, the hypermassive star clusters and the galactic cores are obscured because of dust extinction although the resolution is enough to observe them. On the other hand, in the H - and ground-based K -band images, dust extinction becomes weaker although the clusters and the galactic cores are not resolved. In the K -band

image by $JWST$ or ground-based 8 m telescopes with AO, the clusters and the galactic cores are clearly observable since not only is dust extinction small but also they are resolved. When dust extinction is significant in I band, we need observations by $JWST$ or ground-based 8 m telescopes with AO.

5. CONCLUSIONS AND DISCUSSION

We have performed high-resolution N -body/SPH simulations of merging galaxies. We found that hypermassive star clusters with $\sim 10^8 M_\odot$ form from disturbed gas disks in the central region ($\sim kpc$). In these clusters, active star formations take place, so that some bright core structures appear in the merging galaxy. The features of the hypermassive star clusters formed agree with the observations of ULIRGs with multiple nuclei. Although dust extinction may obscure the clusters after their

formation, the clusters become optically thin within the ULIRG lifetime. These results indicate that one major merger of two spiral galaxies can explain complex structures of multiple nuclei in ULIRGs. Rare multiple major merger events on a short timescale are not necessary.

In the high-redshift universe, gas-rich major mergers must occur frequently. Our result suggests that these merging galaxies have multiple hypermassive star clusters that would be observed as bright sources in either near- or far-infrared bands. Future observations using, e.g., *JWST* or ground-based 8 m telescopes with AO are expected to find a number of such merging galaxies with multiple bright sources.

In our simulations, we assume that the main feedback source is Type II SNe and radiative feedback from newly formed stars is not taken into account. If the radiative feedback is effective, gas in hypermassive star clusters is heated and is ejected from the cluster (Krumholz & Dekel 2010). This effect may reduce the cluster mass. In order to study this effect, we need radiation-hydrodynamic simulations as performed by Krumholz et al. (2011).

Since the hypermassive star clusters are compact ($\sim 10^8 M_\odot$ within 20–30 pc), it is possible that star–star collisions and merging occur in these clusters (Portegies Zwart et al. 1999). If the stellar mass loss in the main-sequence phase is not very large, such merging of stars might result in the runaway growth of supermassive stars and the formation of intermediate-mass black holes (IMBHs; Ebisuzaki et al. 2001; Portegies Zwart et al. 2004). These IMBHs are carried to the center of the galaxy together with the parent hypermassive star cluster by dynamical friction. If there is already a supermassive black hole (SMBH) at the center of the progenitor galaxies, the IMBH merges with the SMBH through dynamical friction and eccentricity evolution (Matsubayashi et al. 2007). If there is no SMBH, multiple IMBHs conveyed to the center by the parent cluster finally merge with each other to form the seed of a SMBH.

The authors thank the anonymous referee for many useful comments. The authors also thank Junichi Baba, Nozomu Kawakatu, Masakazu A. R. Kobayashi, and Tohru Nagao for helpful discussions. Numerical computations were carried out on the Cray XT4 and GRAPE system at Center for Computational Astrophysics (CfCA) of National Astronomical Observatory of Japan. This project is supported by NEC Corporation, Molecular-Based New Computational Science Program of NINS, Grant-in-Aid for Scientific Research (17340059) of JSPS, and HPCI Strategic Program Field 5 “The origin of matter and the universe.” T.R.S. is financially supported by a Research Fellowship from the Japan Society for the Promotion of Science for Young Scientists. T.O. is financially supported by Grant-in-Aid for Scientific Research (S) by JSPS (20224002) and by Grant-in-Aid for Young Scientists (21840015).

REFERENCES

- Alonso-Herrero, A., García-Marín, M., Monreal-Ibero, A., et al. 2009, *A&A*, **506**, 1541
- Alonso-Herrero, A., García-Marín, M., Rodríguez Zaurín, J., et al. 2010, *A&A*, **522**, A7
- Athanassoula, E., Makino, J., & Bosma, A. 1997, *MNRAS*, **286**, 825
- Barnes, J. E. 1992, *ApJ*, **393**, 484
- Barnes, J. E., & Hernquist, L. 1992, *Nature*, **360**, 715
- Barnes, J. E., & Hernquist, L. 1996, *ApJ*, **471**, 115
- Bekki, K., & Shioya, Y. 2000, *ApJ*, **542**, 201
- Borne, K. D., Bushouse, H., Lucas, R. A., & Colina, L. 2000, *ApJ*, **529**, L77
- Bournaud, F., Chapon, D., Teyssier, R., et al. 2011, *ApJ*, **730**, 4
- Bournaud, F., Duc, P., & Emsellem, E. 2008, *MNRAS*, **389**, L8
- Bournaud, F., Elmegreen, B. G., & Elmegreen, D. M. 2007, *ApJ*, **670**, 237
- Bushouse, H. A., Borne, K. D., Colina, L., et al. 2002, *ApJS*, **138**, 1
- Colina, L., Arribas, S., & Monreal-Ibero, A. 2005, *ApJ*, **621**, 725
- Covington, M. D., Kassin, S. A., Dutton, A. A., et al. 2010, *ApJ*, **710**, 279
- Cox, T. J., Dutta, S. N., Di Matteo, T., et al. 2006, *ApJ*, **650**, 791
- Cui, J., Xia, X., Deng, Z., Mao, S., & Zou, Z. 2001, *AJ*, **122**, 63
- Di Matteo, P., Combes, F., Melchior, A., & Semelin, B. 2007, *A&A*, **468**, 61
- Draine, B. T. 2003, *ApJ*, **598**, 1017
- Ebisuzaki, T., Makino, J., Tsuru, T. G., et al. 2001, *ApJ*, **562**, L19
- Farrah, D., Bernard-Salas, J., Spoon, H. W. W., et al. 2007, *ApJ*, **667**, 149
- Fioc, M., & Rocca-Volmerange, B. 1999, arXiv:astro-ph/9912179
- García-Marín, M., Colina, L., & Arribas, S. 2009a, *A&A*, **505**, 1017
- García-Marín, M., Colina, L., Arribas, S., & Monreal-Ibero, A. 2009b, *A&A*, **505**, 1319
- Hernquist, L. 1992, *ApJ*, **400**, 460
- Hernquist, L. 1993, *ApJ*, **409**, 548
- Hinz, J. L., & Rieke, G. H. 2006, *ApJ*, **646**, 872
- Immeli, A., Samland, M., Gerhard, O., & Westera, P. 2004, *A&A*, **413**, 547
- Kazantzidis, S., Mayer, L., Colpi, M., et al. 2005, *ApJ*, **623**, L67
- Kim, D., Veilleux, S., & Sanders, D. B. 2002, *ApJS*, **143**, 277
- Kim, J., Wise, J. H., & Abel, T. 2009, *ApJ*, **694**, L123
- Kobayashi, M. A. R., Totani, T., & Nagashima, M. 2010, *ApJ*, **708**, 1119
- Kormendy, J., Fisher, D. B., Cornell, M. E., & Bender, R. 2009, *ApJS*, **182**, 216
- Krumholz, M. R., & Dekel, A. 2010, *MNRAS*, **406**, 112
- Krumholz, M. R., Klein, R. I., & McKee, C. F. 2011, *ApJ*, **740**, 74
- Li, Y., Mac Low, M., & Klessen, R. S. 2004, *ApJ*, **614**, L29
- Matsubayashi, T., Makino, J., & Ebisuzaki, T. 2007, *ApJ*, **656**, 879
- Mendes de Oliveira, C., & Hickson, P. 1991, *ApJ*, **380**, 30
- Mengel, S., Lehnert, M. D., Thatte, N. A., et al. 2008, *A&A*, **489**, 1091
- Mihos, J. C., & Hernquist, L. 1996, *ApJ*, **464**, 641
- Mihos, J. C., Richstone, D. O., & Bothun, G. D. 1992, *ApJ*, **400**, 153
- Monreal-Ibero, A., Arribas, S., Colina, L., et al. 2010, *A&A*, **517**, A28
- Narayanan, D., Cox, T. J., Hayward, C. C., Younger, J. D., & Hernquist, L. 2009, *MNRAS*, **400**, 1919
- Nardini, E., Risaliti, G., Salvati, M., et al. 2008, *MNRAS*, **385**, L130
- Noguchi, M. 1999, *ApJ*, **514**, 77
- Portegies Zwart, S. F., Baumgardt, H., Hut, P., Makino, J., & McMillan, S. L. W. 2004, *Nature*, **428**, 724
- Portegies Zwart, S. F., Makino, J., McMillan, S. L. W., & Hut, P. 1999, *A&A*, **348**, 117
- Ribeiro, A. L. B., de Carvalho, R. R., & Zepf, S. E. 1994, *MNRAS*, **267**, L13
- Risaliti, G., Maiolino, R., Marconi, A., et al. 2006, *MNRAS*, **365**, 303
- Rodríguez Zaurín, J., Tadhunter, C. N., & González Delgado, R. M. 2010, *MNRAS*, **403**, 1317
- Saitoh, T. R., Daisaka, H., Kokubo, E., et al. 2008, *PASJ*, **60**, 667
- Saitoh, T. R., Daisaka, H., Kokubo, E., et al. 2009, *PASJ*, **61**, 481
- Saitoh, T. R., Daisaka, H., Kokubo, E., et al. 2010, in ASP Conf. Ser. 423, *Galaxy Wars: Stellar Populations and Star Formation in Interacting Galaxies*, ed. B. Smith, J. Higdon, S. Higdon, & N. Bastian (San Francisco, CA: ASP), **185**
- Saitoh, T. R., Daisaka, H., Kokubo, E., et al. 2011, in IAU Symp. 270, *Computational Star Formation*, ed. J. Alves, B. Elmegreen, & V. Trimble (Cambridge: Cambridge Univ. Press), **483**
- Saitoh, T. R., Koda, J., Okamoto, T., Wada, K., & Habe, A. 2006, *ApJ*, **640**, 22
- Saitoh, T. R., & Makino, J. 2009, *ApJ*, **697**, L99
- Saitoh, T. R., & Makino, J. 2010, *PASJ*, **62**, 301
- Salpeter, E. E. 1955, *ApJ*, **121**, 161
- Sanders, D. B., Mazzarella, J. M., Kim, D., Surace, J. A., & Soifer, B. T. 2003, *AJ*, **126**, 1607
- Sanders, D. B., & Mirabel, I. F. 1996, *ARA&A*, **34**, 749
- Sugimoto, D., Chikada, Y., Makino, J., et al. 1990, *Nature*, **345**, 33
- Surace, J. A., Sanders, D. B., Vacca, W. D., Veilleux, S., & Mazzarella, J. M. 1998, *ApJ*, **492**, 116
- Teyssier, R., Chapon, D., & Bournaud, F. 2010, *ApJ*, **720**, L149
- Veilleux, S., Kim, D., & Sanders, D. B. 2002, *ApJS*, **143**, 315
- Whitmore, B. C., & Schweizer, F. 1995, *AJ*, **109**, 960